Advances in Science and Technology Research Journal

Advances in Science and Technology Research Journal, 2026, 20(5), 238–253
https://doi.org/10.12913/22998624/216249
ISSN 2299-8624, License CC-BY 4.0

Received: 2025.12.05
Accepted: 2026.03.15
Published: 2026.04.01

Evaluating material-extrusion additive manufacturing for hydrodynamic clutch rotor prototypes

Wojciech Iwanicki[1], Jarosław Kotliński[2], Karol Osowski[2*], Artur Olszak[3], Ireneusz Musiałek[1], Karol Musiałek[1], Zbigniew Kęsy[1], Andrzej Kęsy[1]

[1] Mechatronics Division, Jan Kochanowski University of Kielce, ul. Żeromskiego 5, 25-369 Kielce, Poland
[2] Faculty of Mechanical Engineering, Casimir Pulaski Radom University, ul. Malczewskiego 29, 26-600 Radom, Poland
[3] Łukasiewicz Research Network – New Chemical Syntheses Institute, al. Tysiąclecia Państwa Polskiego 13a, 24-110 Puławy, Poland
* Corresponding author's e-mail: k.osowski@urad.edu.pl

ABSTRACT

The article presents the results of numerical calculations examining the influence of channel roughness in a hydrodynamic clutch on the transmitted torque. Additionally, the study reports measurements of surface roughness and dimensional deviations of hydrodynamic clutch rotors. The rotors were manufactured using 3D printing based on material extrusion (MEX) technology and produced from three different materials: PLA, ABS, and PET-G. Based on the analysis of the obtained measurement and calculation results, the suitability of the MEX technology for manufacturing hydrodynamic clutch rotor prototypes is assessed. The results indicate that the surface roughness of the printed rotors is comparable to that of rotors produced by casting or machining. Moreover, the dimensional accuracy of the printed rotors lies within the tolerance range specified in the design of hydrodynamic clutch rotors. The article concludes with findings indicating that the adopted modeling and manufacturing procedure, employing the MEX technology, can be applied to produce hydrodynamic clutch rotor prototypes.

Keywords: hydrodynamic clutch rotor prototypes, 3D printing, MEX technology, surface roughness, dimensional accuracy, mathematical modeling

INTRODUCTION

Hydrodynamic clutches (HC) are mechanical components used in drive systems of machines exposed mainly to dynamic overloads. The primary function of the HC is to transmit torque from the drive motor to the machine's working system. HC are used in single- and multi-drive systems: pumps, compressors, conveyors, vehicles, working machinery, etc. [1]. The wide application of HC in various machines is due to their specific design, in which the input and output shafts are not mechanically connected.

The new requirements placed on drive systems containing a HC in their structure mean that new, more effective design solutions for these components are being sought. New requirements for drive systems that incorporate hydrodynamic clutches have led to a search for new and more effective design solutions for these components. The most promising directions in this research include improving HC control through the use of working fluids with variable rheological properties. Another key focus is enhancing clutch performance by increasing the manufacturing accuracy of rotors using 3D printing. The use of working fluids with variable rheological properties, such as electrorheological or magnetorheological fluids, enables the control of HC by means of electric current [2–5].

The suitability of 3D printing for manufacturing rotors was demonstrated in [6], which addressed a hydrodynamic transmission with a rotor structure similar to that of hydrodynamic

clutch rotors. However, the limitations of the widespread application of 3D printing for HC rotor manufacturing may be the surface roughness and the dimensional accuracy of the rotors' working spaces. The roughness of the working space of the rotors is particularly important due to the increasing resistance to the flow of the working fluid with increasing roughness. Geometric errors in the rotor design may, in turn, cause deviations from the HC characteristics assumed during design.

HC rotors are currently manufactured by casting, plastic forming or machining [7]. In mass production, HC rotors with both spatially shaped and radial blades are typically manufactured using centrifugal casting, most often in permanent molds. Casting methods are characterized by relatively high surface roughness *Rz*, ranging from 10 μm to 100 μm. The main disadvantage of centrifugal casting methods lies in geometric inaccuracies arising from core distortion, core misplacement within the mold, or deformation of core supports during metal pouring. Plastic forming and machining allow for obtaining a surface roughness *Rz* ranging from 5 μm to 80 μm. However, applying this type of machining requires dividing the rotor into separate components to ensure tool access to the machined surfaces of the working space. It is assumed that the manufacturing deviations of HC rotors should not exceed 0.1 mm.

The use of 3D printing will enable the production of HC rotors of any shape from various construction materials, including metals. In the case of metal printing, the dimensions of the printer's working chamber may currently be limiting factor, due to the external diameters of the rotors reaching up to 1 m. 3D printing can be performed using various technologies, such as selective laser melting (SLM), fused deposition modeling (FDM), stereolithography (SLA), and laminated object manufacturing (LOM) [8–12]. A characteristic feature of 3D printing is that each method requires specifically dedicated materials [13–16].

Several parameters are used to assess the quality of machine components, the most important of which are:

- surface roughness,
- geometric accuracy.

Research on the surface quality of components produced using FDM technology constitutes a significant area of study within additive manufacturing. Surface roughness is a key quality parameter that influences the functional performance of the fabricated parts. The literature highlights that the inherent layer-by-layer nature of the FDM process results in a "stair-stepping" effect on inclined and geometrically complex surfaces, substantially affecting the surface roughness of the final components [17]. The surface roughness value in 3D printing ranges from 3 μm to 150 μm and depends on the 3D printing method, the material used and the type of 3D printer. To reduce surface roughness, printed parts can be additionally processed: mechanically, thermally, chemically or painted [18–20]. Dimensional deviations in geometry that occur during the 3D printing process depend on multiple factors. These include the printing method, the material used, the type of 3D printer, the discretization process during conversion from CAD to STL, and the selected printing parameters such as layer thickness, infill, positioning of the part in the printer's working area, and the adopted support structure [21–24]. Despite the wide range of studies on process parameters and surface roughness control of components produced using FDM technology [25–28], the literature lacks publications dedicated to the specific relationship between the surface roughness of parts and flow-related studies, such as the analysis of flow resistance in printed channels or the impact of surface roughness on hydrodynamic operating conditions. Currently, the measurement of part geometry deviations is performed using optical measuring systems [29–30].

This article evaluates the effect of surface roughness on the torque transmitted by a HC using a mathematical model. It also presents measurements of roughness and geometric deviations in HC rotors produced by MEX technology with three materials: PLA, ABS, and PET-G. The presented research contributes to increasing the level of knowledge in the field of new methods of manufacturing HC rotor prototypes.

RESEARCH OBJECT

The research focused on a prototype HC intended for a home wind farm [31]. The HC contained a pump rotor mounted on the input shaft and a turbine rotor mounted on the output

shaft. The pump rotor and the turbine rotor formed a working space filled with the working fluid. Driven by the motor, the pump rotor rotates at an angular velocity ω_1. This motion induces swirling of the working fluid within the channels, which, under the influence of centrifugal force, flows toward the turbine rotor. The fluid stream flowing out of the pump rotor strikes the turbine rotor blades, causing the rotor to rotate at an angular velocity ω_2 and transferring the torque M from the input shaft to the output shaft.

The HC characteristic used in drive system design is the dependence of the transmitted torque M on the kinematic ratio i_k, expressed as:

$$M = f(i_k) \tag{1}$$

where: $i_k = \omega_2/\omega_1$ – kinematic ratio.

Each rotor consists of radial blades mounted between the walls of the housing. Channels formed between the blades and the rotor housing constitute the working space, where the fluid circulates [32]. A channel is formed by two adjacent blades and the outer and inner casing of the rotor. Figure 1 presents the meridional cross-section obtained by intersecting the HC with a plane passing through the rotor axis, which is identical for both the pump and turbine rotors.

The dimensions of the pump and turbine rotors are presented in Table 1. The prototype HC intended for testing was assumed to be manufactured using 3D printing. The work [32] demonstrates that rotors with the dimensions given in Table 1, produced from plastics via 3D printing, meet the mechanical strength requirements.

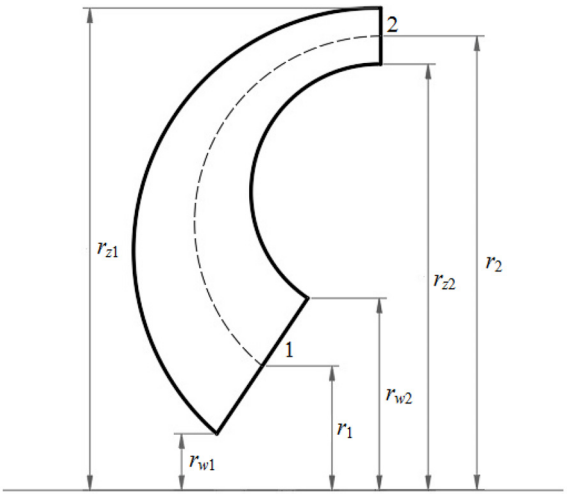

Figure 1. Meridional cross-section of pump rotor and turbine rotors

INFLUENCE OF SURFAE ROUGHNESS ON TORQUE TRANSMITTED BY A HC

Mathematical model of a hydrodynamic clutch

To determine the influence of surface roughness in the HC rotor channels on the transmitted torque, a one-dimensional mathematical model of the HC was employed [33–35]. The main disadvantage of the one-dimensional model is its low accuracy, resulting from the use of several basic parameters to describe the HC geometry. To improve the model's accuracy, verification based on experimental research is performed. This model is based on the mean jet flowing along the mean line of the blade channel. Existing two- and three-dimensional mathematical models are mainly used for simulation purposes, as they can be applied to HCs with precisely defined geometry [36, 37]. The one-dimensional mathematical model of the HC consists of equations for the torques acting on the pump and turbine rotors, as well as an energy balance equation expressed as the sum of head rises [38].

To formulate the mathematical model of the HC on the rotor's meridional cross-section, points 1 and 2 are identified on the mean line of the channel. These correspond, respectively, to the entry and exit of the fluid stream in the rotor. At each of these points, the distribution of absolute velocity c of the fluid is assumed as

Table 1. Dimensions of the pump and turbine rotors

Meridional cross-section dimensions [mm]		
Effective radius of HC. Outer radius of the pump rotor outlet and inlet radius of the turbine rotor	r_{z1}	123.3
Outer radius of the pump rotor outlet and turbine rotor inlet	r_{z2}	107.1
Inner radius of pump rotor inlet and turbine rotor outlet	r_{w1}	50.9
Outer radius of pump rotor inlet and turbine rotor outlet	r_{w2}	78.4
Channel dimensions [mm]		
Channel height	h	16.2
Channel width	b	72.5

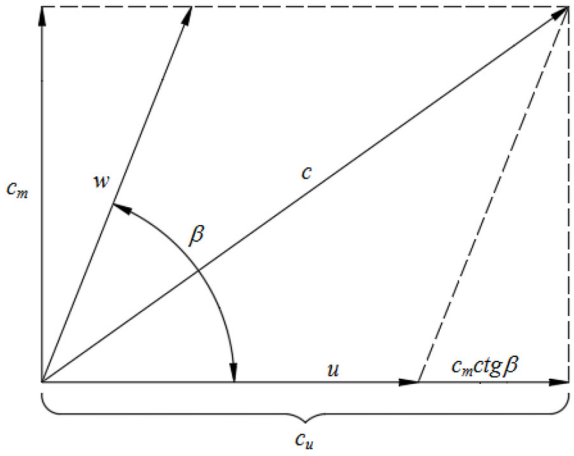

Figure 2. Velocity distribution of the fluid flowing in the rotor channel

shown in Figure 2. The following notations are used: u – tangential speed, w – relative speed, c_u – peripheral speed, c_m – meridional speed, β – angle between relative speed and peripheral speed.

The meridional speed c_m is the same in both rotors, while the other speeds are denoted by two indices: the first refers to the rotor, and the second to the rotor's inlet or outlet.

The torque on the HC rotors is caused by the peripheral speed c_u, therefore the hydraulic torques M of the HC pump and turbine rotors are equal in value and amount to:

$$\begin{aligned} M_1 &= \rho Q\,[c_{u12} r_2 - c_{u22} r_1] \\ M_2 &= \rho Q[c_{u22} r_1 - c_{u12} r_2] \end{aligned} \tag{2}$$

where: $M = M_1 = -M_2$, Q – working fluid flow rate, r – density of the working fluid, r_1 – fluid inlet radius of the rotor, r_2 – fluid outlet radius of the rotor.

The head balance equation can be written as:

$$h_1 - h_2 - h_u - h_t = 0 \tag{3}$$

where: h_1 – pump rotor lifting height, h_2 – turbine rotor lifting height, h_u – head loss due to the impact of the fluid on the rotor blades at the inlet, h_t – head loss due to fluid friction against the walls of the rotor channels.

The head rises of the pump and turbine rotors are defined by the following equations:

$$\begin{aligned} h_1 = \frac{\omega_1 r_2}{g}[(u_{12} + c_m ctg\beta_{12}) \; - \\ -(u_{22} + c_m ctg\beta_{22})\rho_3] \end{aligned} \tag{4}$$

$$h_2 = h_1 i_k \tag{5}$$

where: g – acceleration of gravity.

The impact losses h_u are described by the formula:

$$h_u = \zeta_1 \frac{c_{u1}^{\;2}}{2g} + \zeta_2 \frac{c_{u2}^{\;2}}{2g} \tag{6}$$

where: c_u – the impact velocity of the working fluid on the blades at the inlet to the rotors, ζ – impact loss factor.

The friction losses h_t are described by the formula:

$$\begin{aligned} h_t = \phi \frac{c_m^{\;2}}{2g} \\ (ctg^2\beta_{12} + ctg^2\beta_{22} + 2) \end{aligned} \tag{7}$$

where: φ –friction loss coefficient in the rotor.

The friction loss coefficient φ is obtained from the formula:

$$\varphi = \lambda \frac{l}{2r_h} \kappa \tag{8}$$

where: λ – linear resistance coefficient, l – length of the mean stream line; r_h – hydraulic radius, k – coefficient of increased flow resistance due to the rotational motion of the channels, determined by the blade angles.

The coefficient λ is calculated on the basis of the following formula [39]:

$$\frac{1}{\sqrt{\lambda}} = -2 \cdot lg\left(\frac{6{,}1}{Re^{0{,}91}} + 0{,}268\,\varepsilon\right) \tag{9}$$

where: Re – Reynolds number, ε – relative roughness of the channel surface.

The Reynolds number appearing in formula (8) is determined by the relationship:

$$Re = \frac{\omega_1 (1 - i_k) r_{z1}}{v} \tag{10}$$

where: ω_1 – angular speed of the pump rotor, i_k – kinematic ratio, r_{z1} – pump rotor radius, v – kinematic viscosity of the working fluid, and the relative roughnesse is determined by the relation:

$$\varepsilon = \frac{Rz}{2\,r_h} \tag{11}$$

where: Rz – roughness parameter, r_h – hydraulic radius of the channel.

Hydraulic radius r_h is determined by the formula:

$$r_h = \frac{bh}{(2h+2b)} \tag{12}$$

where: h – rotor channel height, b – rotor channel width.

Calculation results

Calculations of the influence of surface roughness in the HC rotor channels on the transmitted torque M were performed. The calculations used a flow resistance increase coefficient recommended for this HC type, $\kappa = 25$, impact loss coefficient $\zeta_1 = \zeta_2 = 1$ [40–43] and the selected angular velocity $\omega_1 = 100$ rad/s. It was assumed that the cross-section is constant along the entire length of the channel in which the working fluid flows, and that the HC is filled with HL 46 oil whose kinematic viscosity is $\nu = 14 \times 10^{-6}$ m^2/s and its density is $\rho = 880$ kg/m^3.

The calculations started with determining the hydraulic diameter of the channel according to formula (12). By substituting the values from Table 1, it was found that $d = 16$ mm. Subsequently, the value of coefficient ε was calculated from formula (11), and the linear resistance coefficient was calculated for each Rz value using formula (9) at the chosen kinematic ratio $i_k = 0$. Table 2 shows the calculated values of the coefficients ε and λ.

The friction loss coefficient φ was calculated from formula (8). For this purpose, Re was calculated from formula (10) and inserted into formula (9) in order to calculate λ. The calculations performed for the assumed values of i_k and for different values of Rz are presented in Table 3.

The calculation of the torque M for individual values of the friction loss coefficient φ, which depends on the roughness Rz, requires solving Equations 2–7 numerically. Delphi software was used to perform the numerical calculations. The calculation procedure used polynomials of the form $\varphi = f(i_k)$, derived from the data in Table 3. The formulas of these polynomials are presented in Table 4.

Figure 3 shows the polynomials' curves $\varphi = f(i_k)$ presented in Table 4. Finally, Figure 4 shows the dependence of the torque M on the kinematic ratio i_k for selected roughness values of Rz.

To assess the influence of channel roughness on the decrease of torque M, calculations were performed for two roughness values: 5 μm (typical of machining) and 100 μm (typical of casting). The results were compared at an input shaft angular velocity $\omega_1 = 100$ rad/s. The results are presented in Table 5.

Figure 5 additionally illustrates the losses caused by increasing the channel roughness from 5 μm to 10 μm, 35 μm, 40 μm, 50 μm, 100 μm, respectively. The results were compared at an input shaft angular velocity $\omega_1 = 100$ rad/s.

Table 2. Value of coefficients ε and λ for individual Rz for $i_k = 0$

Rz [μm]	ε [-]	λ [-]
5	$3.13 \cdot 10^{-4}$	$1.5 \cdot 10^{-2}$
10	$6.25 \cdot 10^{-4}$	$1.8 \cdot 10^{-2}$
40	$2.50 \cdot 10^{-3}$	$2.5 \cdot 10^{-2}$
50	$3.13 \cdot 10^{-3}$	$2.6 \cdot 10^{-2}$
100	$6.25 \cdot 10^{-3}$	$3.3 \cdot 10^{-2}$

Table 4. Formulas defining the relationship $\varphi = f(i_k)$ for the determined values of Rz.

Value of Rz [μm]	Formula $\varphi = f(i_k)$
$Rz = 5$	$\varphi = 0.0061\, i_k^2 + 1.278\, i_k + 3.6532$
$Rz = 10$	$\varphi = 0.0101\, i_k^2 + 0.0538\, i_k + 4.3569$
$Rz = 40$	$\varphi = 0.0109\, i_k^2 - 0.0109\, i_k + 6.2209$
$Rz = 50$	$\varphi = 0.0059\, i_k^2 + 0.0131\, i_k + 6.5971$
$Rz = 100$	$\varphi = 0.0042\, i_k^2 + 0.0083\, i_k + 8.1265$

Table 3. Friction loss coefficient φ for the assumed values of Rz and i_k

i_k [-]	Rz [μm]				
	5	10	40	50	100
0	3.7500	4.3963	6.2066	6.6056	8.1318
0.2	4.0118	4.5562	6.2769	6.6680	8.1744
0.4	4.0800	4.6041	6.2690	6.6876	8.1878
0.6	4.2004	4.6911	6.3403	6.7241	8.2130
0.8	4.4791	4.9025	6.4473	6.8192	8.2789

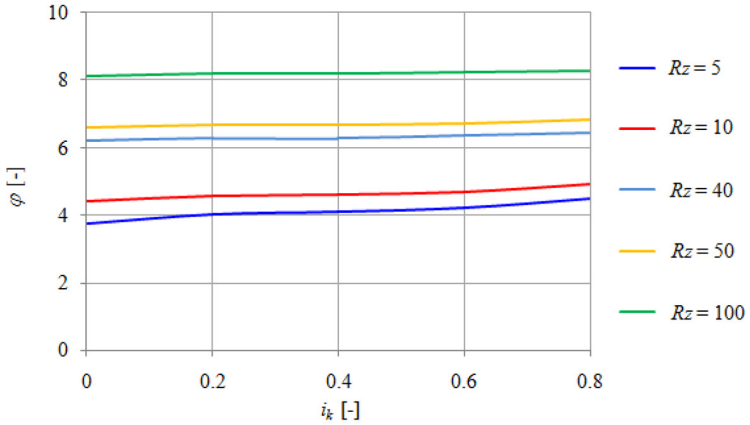

Figure 3. Polynomial curves $\varphi = f(i_k)$ for selected values of Rz

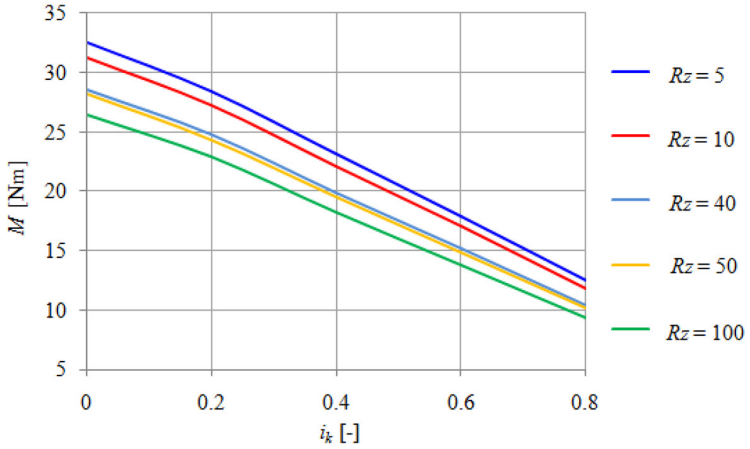

Figure 4. The relationship $M = f(i_k)$, for different values of Rz

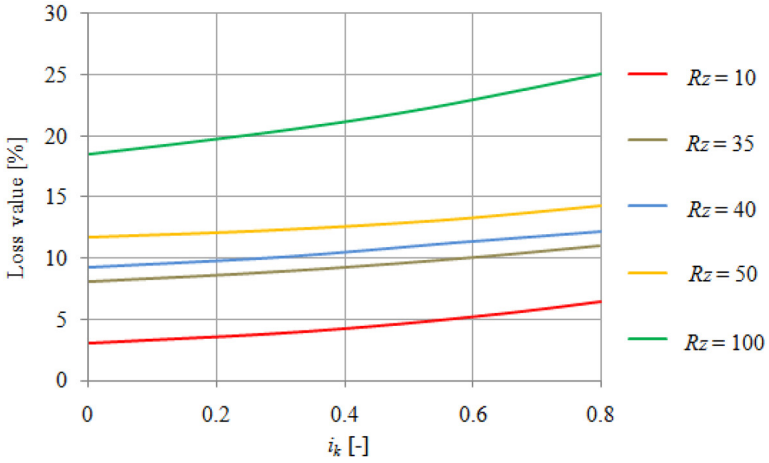

Figure 5. Torque losses due to increased channel roughness

Table 5. Values of transmitted torques M at the angular velocity of the input shaft ω_1 = 100 rad/s

ω [rad/s]	i_k [-]	M [Nm] for Rz = 5 μm	M [Nm] for Rz = 100 μm	Loss value [Nm]	Loss value [%]
100	0	32.48	26.45	6.03	18.6
	0.2	28.40	22.85	5.55	19.5
	0.4	23.11	18.25	4.86	21.0
	0.6	17.89	13.82	4.07	22.8
	0.8	12.49	9.38	3.11	24.9
	Average value			4.72	21.4

TESTING THE PRINT QUALITY OF HC ROTOR CHANNELS

Channel printing

To facilitate access to the entire surface of the HC rotor channel during measurements, a measurement template was printed. This template consisted of a fragment of the rotor, including one blade and parts of the rotor housing. The solid model of the measurement template was created using Inventor Professional. The template is shown in Figure 6.

The positioning of the measurement template on the printer's working platform, along with the required supports, is shown in Figure 7.

To reduce printing material costs and shorten printing time, the measuring template was designed not as a solid part, but with an internal filling with a grid structure. A view of the measuring device with visible walls, supports and filling structure is shown in Figure 8.

The measurement template was printed using Double P255 3D printer manufactured by 3DGence. It uses MEX technology and is equipped with two print heads and a material flow control system. The basic materials used in this technology are ABS, PLA and PET-G plastics. The properties of these materials, developed based on commercial product offerings, are presented in Table 6.

The selection of printing parameters on the Double P255 3D printer was carried out in accordance with the printer manufacturer's recommendations, separately for each printed material, using 3DGence Slicer 4.0. The values of the selected 3D printing parameters specified for the materials used are presented in Table 7.

The measurement template was printed from filaments made of PLA, ABS and PET-G materials. Each of these materials is available in several filament types, distinguished by color, which exhibit slight variations in mechanical properties and print quality. In order to account for the filament types in the study, four filament variants were selected for each material, and the measurement template was printed. Figure 9 shows printouts of the measurement template in the color of the filament used. In this way, four measurement templates of different colors were obtained for each material.

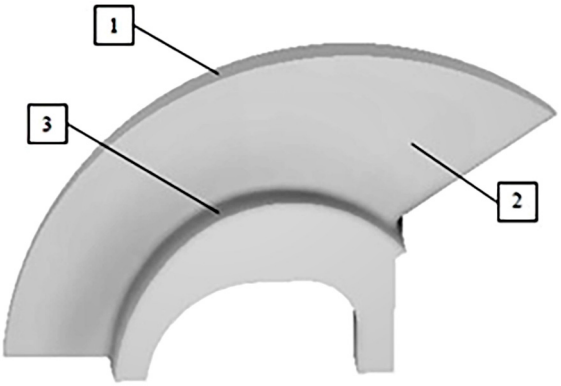

Figure 6. Measurement template:
1 – contact surface with the wall of the outer housing,
2 – active surface of the blade,
3 –inner wall of the housing

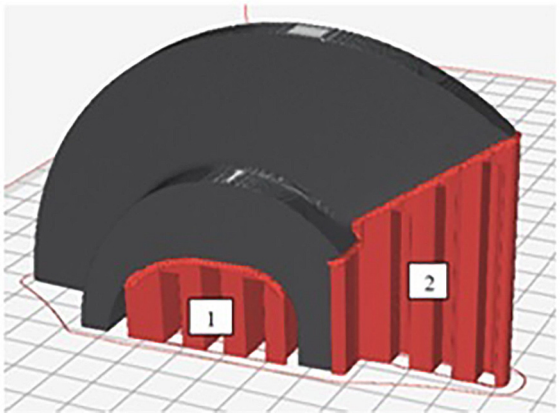

Figure 7. Positioning of the measurement template on the working platform: 1 – inner housing support, 2 – blade support

Table 6. The basic properties of materials used in the MEX technology [44]

Material constants		Values		
		PLA	ABS	PET-G
Mechanical	Tensile strength R_m [MPa]	110–145	44	50
	Elongation at break A [%]	5.2	9	7.5
	Izod impact strength [kJ/m^2]	7.5	36	86
	Young's modulus [GPa]	3.3–3.9	2	2
Physical	Melting point [°C]	200–220	235–255	230–255
	Softening point [°C]	60	103	103

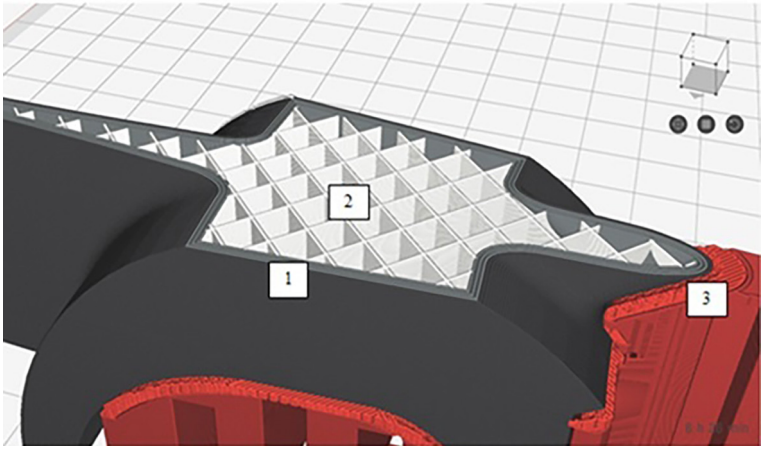

Figure 8. View of the measurement template showing the internal structure: 1 – model walls, 2 – grid-like filling structure, 3 – supports

Surface roughness measurement of the measuring template

The *Ra* and *Rz* parameters are related but describe the surface shape in different ways, so usually both are measured. *Ra* is the basic indicator of surface quality, and *Rz* is a supplement in production quality control. However, in the considerations regarding the influence of roughness on flow resistance in channels, only *Rz* is taken into account [39]. For each printed measurement template, three roughness measurements were performed on the active blade surfaces along the mean line, using the *Ra* and *Rz* parameters. The measurements were performed on a 5 mm-long section of the active blade surface, depending on

Table 7. Printing parameters of printer 3D Double P255 for PLA, ABS, PET-G materials

Printer parameters for 3D Double P255	Value		
	PLA	ABS	PET-G
Nozzle diameter [mm]	0.4	0.4	0.4
Layer thickness [mm]	0.15	0.15	0.25
Material temperature [°C]	215	260	235
First layer adhesion type	Skirt	Raft	Raft

Figure 9. Measuring template printed using the MEX technology from PLA, ABS, PET-G materials for various types of filaments for each material

the print layer orientation, in the following directions (Figure 10):

- parallel – measurement 1,
- at a 45° angle – measurement 2,
- perpendicular – measurement 3.

Measurements were conducted on the active side of the blade, as this region is subject to the greatest load and experiences the highest fluid flow intensity.

The measurements were carried out using a Mitutoyo Surftest SJ-210 roughness meter, using the differential-inductive method, Figure 11.

The roughness measurement parameters *Rz* and *Ra* are presented in Table 8.

Surface roughness measurement results

The results of the *Rz* and *Ra* roughness measurements of the active part of the blade are presented in Tables 9–11.

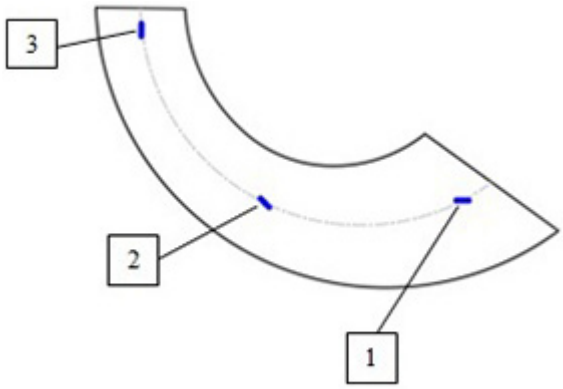

Figure 10. Distribution of measurement sections on the active surface of the blade

Figures 12–14 show the averaged results of the *Rz* and *Ra* roughness measurements.

Method for assessing the geometric accuracy of research models

The accuracy of the measurement standard geometry was assessed for the active surface of the blade. Measurements were performed using the Universe 5 Mpx optical system, which operates on a non-contact measurement method. The measurement system consisted of a 3D scanner and a station with Smarttech 3 Dmeasure software. The measuring station for assessing geometric accuracy is shown in Figure 15. The basic parameters for measuring geometric accuracy are presented in Table 12.

The geometric accuracy was assessed by the deviations of points from the corresponding points on the blade solid model, as recorded by the scanner. During scanning, the measurement resolution, i.e., the minimum value the 3D scanner can distinguish and record, was 0.02 mm. The deviation limit, defining when the difference between the nominal model and the actual dimension is acceptable or critical, was ±0.5 mm. As a result of the blade scanning

Table 8. Surface roughness measurement parameters of blade models

Parameter	Value
Measurement section [mm]	5
Measurement speed [mm/s]	0.5
Detector measuring tip radius [μm]	2
Cut-off wavelength λc (cut-off) [mm]	0.8
Shortwave filter λs (low-pass) [μm]	2.5

Figure 11. A view on roughness meter Mitutoyo Surftest SJ-210 during the: 1 – roughness meter, 2 – detector, 3 – assessed measurement template, 4 – clamp

Table 9. Measured roughness values *Rz* and *Ra* of the PLA measuring template

Measurement No.	Values							
	PLA Natural		PLA Green Grass		PLA Orange		PLA White	
	Rz [μm]	*Ra* [μm]	*Rz* [μm]	*Ra* [μm]	*Rz* [μm]	*Ra* [μm]	*Rz* [μm]	*Ra* [μm]
1	26.794	5.497	12.446	3.049	18.459	4.108	21.246	4.708
2	49.734	10.414	47.324	10.726	48.510	10.836	50.915	11.337
3	41.832	9.915	44.174	9.798	46.339	10.379	43.942	9.804
Average value	39.453	8.608	34.648	7.857	37.769	8.441	38.701	8.616

Table 10. Measured roughness values *Rz* and *Ra* of the ABS measuring template

Measurement No.	Values							
	ABS Natural		ABS Blue		ABS Red		ABS White	
	Rz [m]	*Ra* [μm]	*Rz* [μm]	*Ra* [μm]	*Rz* [μm]	*Ra* [μm]	*Rz* [μm]	*Ra* [μm]
1	18.824	3.133	14.774	2.536	24.425	5.345	16.040	3.259
2	48.389	10.229	48.727	10.218	49.009	10.868	46.498	10.014
3	46.348	9.979	46.127	9.895	47.021	10.150	44.911	9.628
Average value	37.853	7.780	36.542	7.549	40.151	8.787	35.816	7.633

Table 11. Measured roughness values *Rz* and *Ra* of the PET-G measuring template

Measurement No.	Values							
	PET-G Natural		PET-G Carbon Black		PET-G Rubin		PET-G Yelow	
	Rz [μm]	*Ra* [μm]	*Rz* [μm]	*Ra* [μm]	*Rz* [μm]	*Ra* [μm]	*Rz* [μm]	*Ra* [vm]
1	22.893	4.499	25.309	4.477	32.538	6.191	19.212	3.827
2	81.204	18.854	82.182	17.194	83.451	18.361	76.042	18.079
3	79.504	18.198	78.636	16.955	78.841	18.100	73.594	17.454
Average value	61.201	13.850	62.042	12.875	64.943	14.217	56.282	13.120

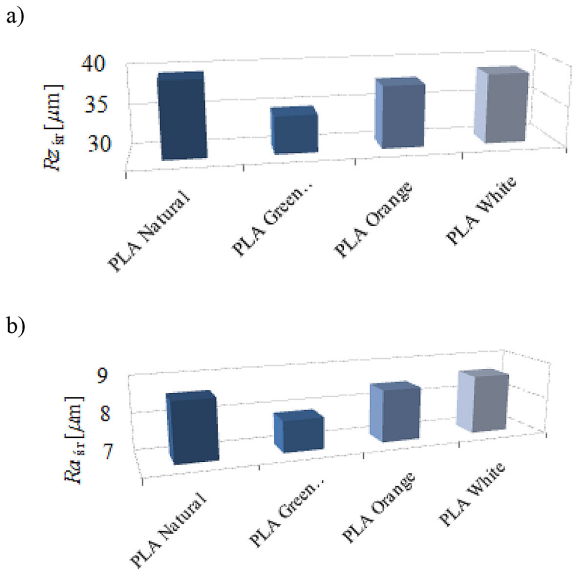

Figure 12. Average roughness values of PLA blades: a – $Rz_{śr}$, b – $Ra_{śr}$

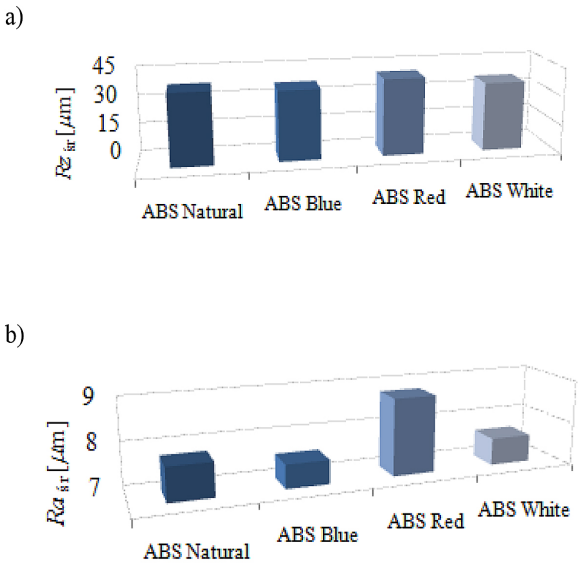

Figure 13. Average roughness values of ABS blades: a – $Rz_{śr}$, b – $Ra_{śr}$

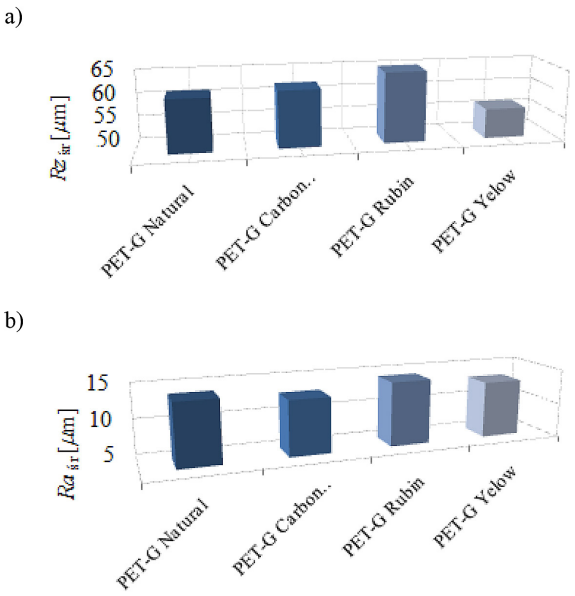

Figure 14. Average roughness values of PET-G blades: a – $Rz_{śr}$, b – $Ra_{śr}$

process, point clouds of over 3 million XYZ coordinates were obtained, defining the geometry of the printed blades.

Results of the geometric accuracy assessment of research models

Figures 16–18 show the measurement results in the form of deviation maps for the active side of the blade of the measuring template made of PLA, ABS, and PET-G materials.

DISCUSSION

The calculation results presented in Table 3 show that friction loss coefficient φ takes maximal value for kinematic ratio $i_k = 0.8$ and roughness Rz = 100 μm. A change in the roughness value Rz from 5 μm to 100 mm at a kinematic ratio of $i_k = 0.8$ results in an almost threefold increase in the friction loss coefficient j. As shown in Figure 4, the $\varphi = f(i_k)$ curves for the assumed Rz values are almost linear and approximately parallel to the X-axis.

The courses of the dependence $M = f(i_k)$, for different values of Rz, shown in Figure 4, indicate a significant influence of the surface roughness Rz on the torque transmitted by the HC. The influence of roughness Rz on the value of the torque M decreases with the increase of kinematic ratio i_k. The data in Table 5 shows that increasing the blade surface roughness from 5 μm to Rz = 100 μm results in a substantial reduction of torque M, averaging 21.4%.

As can be seen from Figure 5, for roughness values from 35 μm to 50 μm, the torque losses M calculated in the presented way are smaller and do not exceed 15%.

The Rz and Ra roughness values for the printed blades (measured and then presented in Tables 9–11) show significant differences depending on the measurement location. The surface roughness values Rz and Ra measured parallel to the layering plane are the lowest, whereas the measurements performed at an angle of 45° to the layering plane have the highest values.

Table 12. Basic parameters for measuring geometric accuracy

Parameter	Value
Scanning technology	White LED structured light
Dimensions of the measuring field [mm]	200 × 300
Distance between measurement points [mm]	0.117
Sampling [pkt/mm^2]	73

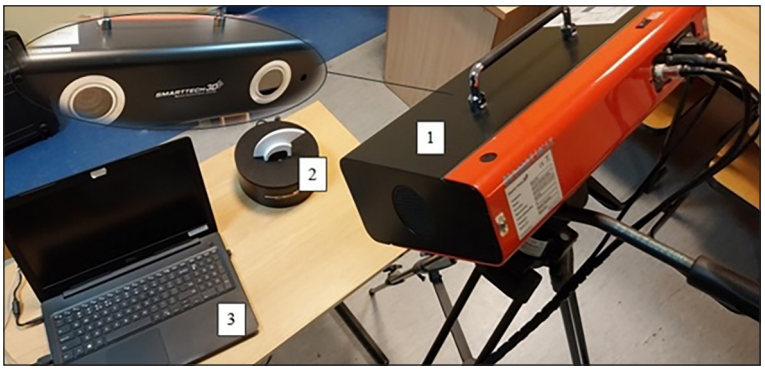

Figure 15. Measuring station for assessing geometric accuracy of the blades: 1–3D scanner, 2 – rotary table on which the measured measuring template is placed, 3 – computer with the software

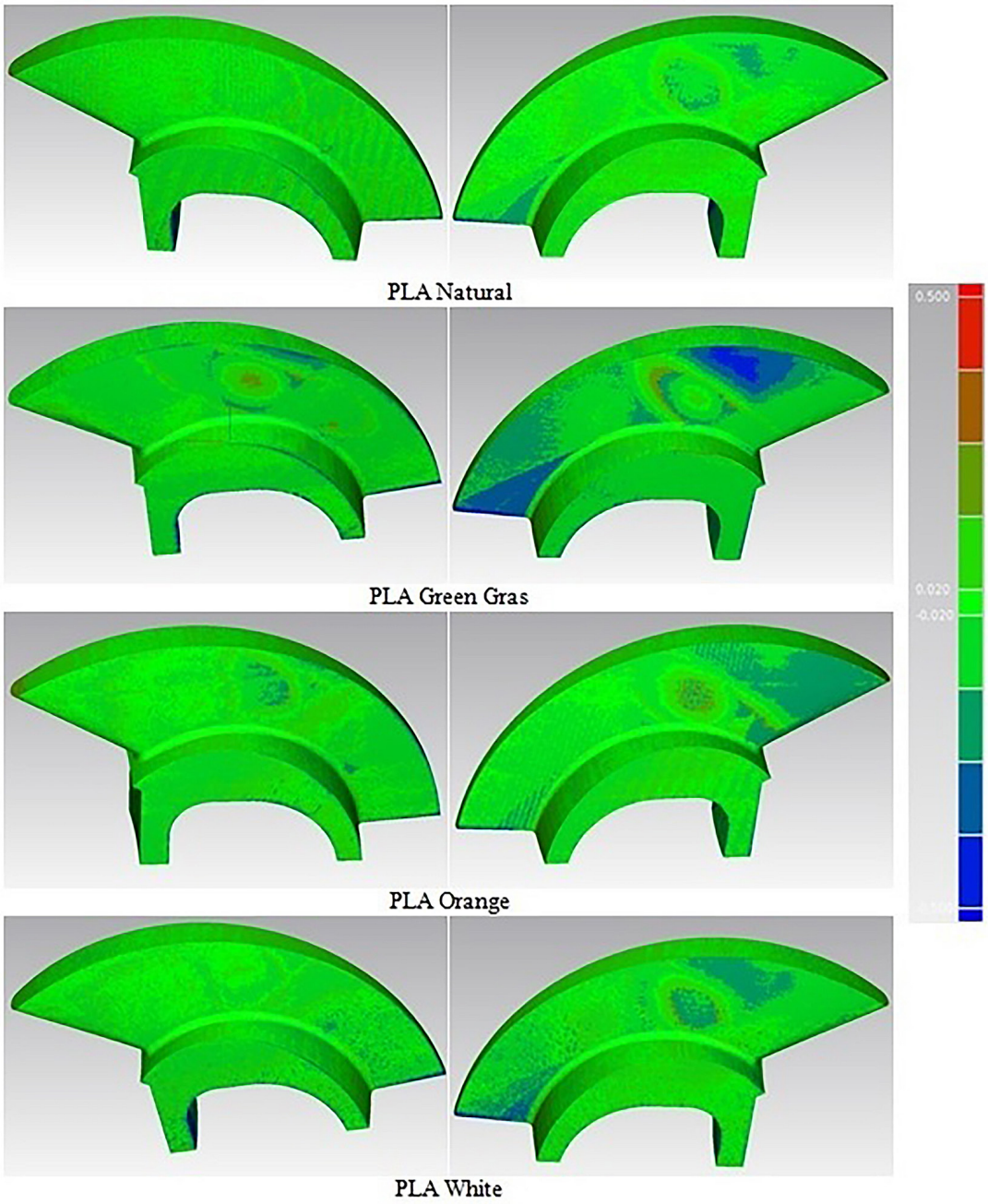

Figure 16. Deviation maps for blades made of PLA material

Figures 12–14 show that the PET-G Rubin material had the highest average roughness ($Rz_{śr}$ = 64.94 μm), whereas the PLA Green Grass material had the lowest average roughness ($Rz_{śr}$ = 34.65 μm). Similarly to the $Rz_{śr}$ roughness, the highest average roughness ($Ra_{śr}$ = 14.22 μm) was obtained for the PET-G Rubin material, and the lowest value ($Ra_{śr}$= 7.54 μm) was obtained for the ABS Blue.

The average difference in *Rz* roughness values for all printed measurement templates between measurement 1 and 2 was 38.25 μm, between measurement 1 and 3 it was 34.85 μm, and between measurement 2 and 3 it was 3.39 μm. The dependence of the obtained roughness values on the measurement location indicates the occurrence of the anisotropy phenomenon. This fact should be taken into account when planning the blades positioning during printing. Furthermore, significant differences can be observed in the roughness values of blades made from materials within the same group. For example, for measurement 1, for blades made of PLA Natural material, roughness is *Rz*

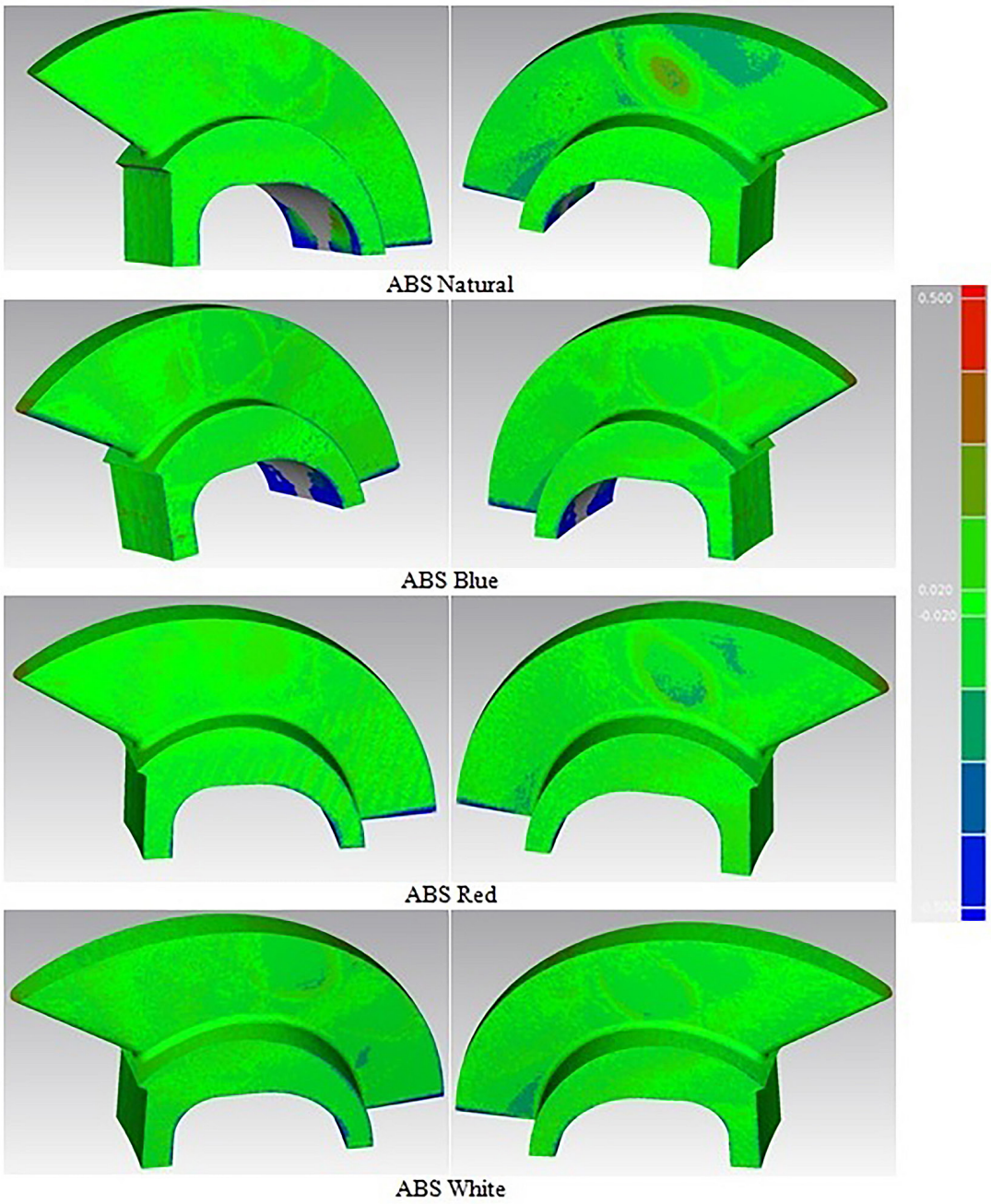

Figure 17. Deviation maps for blades made of ABS material

= 26.79 μm, and for blades made of PLA Green Grass material, roughness is Rz = 12.45 μm.

The geometric accuracy test results presented in Figures 16–18 show that the smallest deviations were obtained for the measuring template made of ABS material. On the side surfaces of most blades, deviations due to material concavities are visible; they do not exceed -0.1 mm. The absence of bulges on the lateral surfaces of the blades indicates that the measurement template was correctly positioned on the working platform and that the model supports were properly designed. The exceedance of critical values in the form of bulges visible on the housing surface and on the blade's dorsal surface, produced from PET-G Rubin material, is likely due to discretization errors typical for curved surfaces. The defects on the edges of the blades visible in Figure 17 are the result of material shrinkage, typical of ABS material. Based on the presented results, it can be concluded that all blades have the required geometric accuracy.

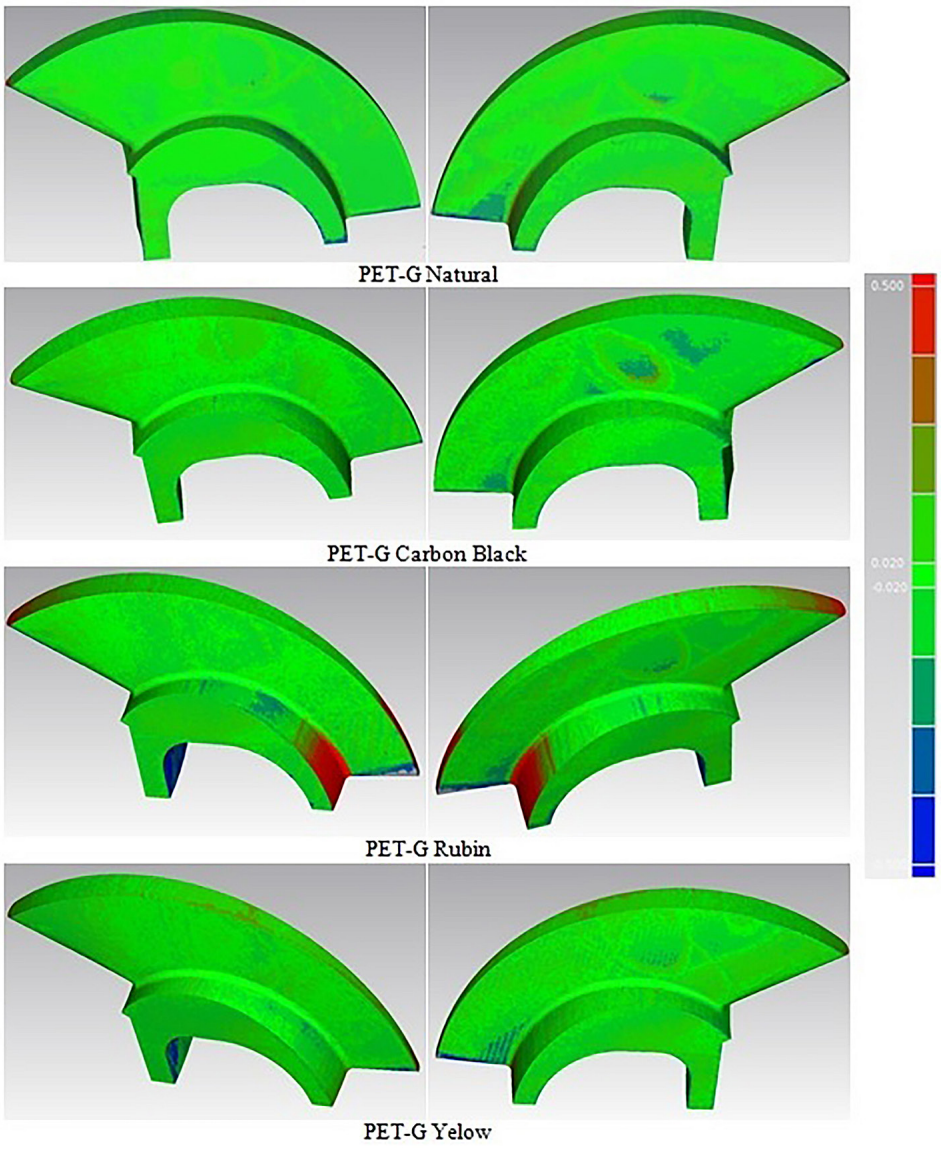

Figure 18. Deviation maps for blades made of PET-G material

CONCLUSIONS

The following conclusions were drawn based on the calculations of the effect of rotor channel roughness on the torque transmitted by the HC, as well as the results of roughness and geometric deviation measurements of HC rotor blades produced using MEX technology from three different materials:

1. Numerical calculations show that the applied mathematical model allows to determine the influence of blade surface roughness on changes in HC torque as a function of the kinematic ratio i_k over a wide range of *Rz* values.
2. The measured surface average roughness *Rz* of channels printed from PLA and ABS does not exceed 40 μm. This value is smaller than the value obtained for rotors manufactured using traditional methods, i.e. casting or machining.
3. The analysis of both the mathematical model calculations and surface roughness measurements indicated that the *Rz* values measured for PLA and ABS materials considered result in torque losses not exceeding 15%. Such losses are within acceptable limits.
4. The employed optical measurement system enable sprecise assessment of the geometric accuracy of the printed rotor channels and the identification of typical technological errors in the manufacturing process.
5. The measurement results of geometric deviations of the measurement templates printed from ABS, PLA, and PET-G showed that these deviations were within the tolerances specified during the design of the HC rotors.

6. The proposed procedure for modeling and manufacturing HC rotors using MEX technology, along with some materials suited for this technology, can be used to produce prototype HC rotors.
7. The obtained research results can be used for experimental testing of HC prototypes with rotors manufactured using 3D printing.

REFERENCES

1. Brun K., Meyenberg C., Thorp J. and Kurz R. Hydrodynamic torque converters for oil and gas compression and pumping applications: basic principles, performance characteristics and applications. In 44th Turbomachinery and 31st Pump Symposia, Houston, Texas, 2015; 1–14
2. Olszak A., Osowski K., Kęsy A., Kęsy Z. Experimental researches of hydraulic clutches with smart fluids. International Review of Mechanical Engineering, 2016; 10(6): 364–372. https://doi.org/10.15866/ireme.v10i6.8421
3. Olszak A., Osowski K., Kęsy Z., Kęsy A. Modelling and testing of a hydrodynamic clutch filled with electrorheological fluid in varying degree. J. Intell. Mater. Syst. Struct., 2019; 30(4): 649–660. https://doi.org/10.1177/1045389X18818780
4. Olszak A., Osowski K., Kesy Z., Kesy A. Investigation of hydrodynamic clutch with a magnetorheological fluid. J. Intell. Mater. Syst. Struct., 2018; 30(1): 155–168. https://doi.org/10.1177/1045389X18803463
5. Madeja J., Kęsy Z., Kęsy A. Application of ER fluid in hydrodynamic clutch. Smart Mater. Struct. 2011; 20, 105005: 1–9. https://doi.org/10.1088/0964-1726/20/10/105005
6. Kotliński J., Migus M., Kęsy Z., Kesy A., Hugo P., Deez B., Schre K., Dimitrov D. Fabrication of hydrodynamic torque converter impellers by using the selective laser sintering method. Rapid Prototyp. J., 2013; 19(6): 430–436. https://doi.org/10.1108/RPJ-04-2011-0043
7. Kęsy A., Computer methods in impellers of hydrodynamic sub-assemblies creation [Metody komputerowe w budowie kół łopatkowych podzespołów hydrokinetycznych]. Radom: Wydawnictwo Politechniki Radomskiej; 2010; 167.
8. Anketa J., Ikshita C., Ishika W., Ankush R., Mir I. Ul H. 3D printing – A review of processes, materials and applications in industry 4.0, Sustainable Oper. Comput., 2022; 3: 33–42. https://doi.org/10.1016/j.susoc.2021.09.004
9. Jiménez M., Romero L., Domínguez I. A., Espinosa M. del Mar, Domínguez M. Additive manufacturing technologies: An overview about 3D printing methods and future prospects, Complexity, 2019; 9656938:1–30. https://doi.org/10.1155/2019/9656938
10. Srinivasan D., Meignanamoorthy M., Ravichandran M., Mohanavel V., Alagarsamy S. V., Chanakyan C., Sakthivelu S., Karthick Alagar, Prabhu T. R., Rajkumar S. 3D printing manufacturing techniques, materials, and applications: An overview, Adv. Mater. Sci. Eng., 2021; 5756563: 1–10. https://doi.org/10.1155/2021/5756563
11. Budzik G., Tomaszewski K. Soboń A. Opportunities for the application of 3D printing in the critical infrastructure system, Energies, 2022; 15. https://doi.org/10.3390/en15051656
12. Paszkiewicz A., Bolanowski M., Budzik G., Przeszłowski Ł., Oleksy M. Process of creating an integrated design and manufacturing environment as part of the structure of industry 4.0, Processes, 2020. https://doi.org/10.3390/PR8091019
13. Su C., Chen Y., Tian S., Lu C., Lv Q. Natural materials for 3D printing and their applications. Gels. 2022; 8(11): 1–39. https://doi.org/10.3390/gels8110748
14. Wyrobek K., Pezda J. The influence of 3D printing parameters on surfaceroughness of thin-walled parts manufactured using FFF technology, Designing, researches and exploitation, 2024; 161–170. https://doi.org/10.53052/9788367652261.16
15. Kamer M. S., Temiz Ş., Yaykasli H., Kaya A., akay O. E. Comparison of mechanical properties of tensile test specimens produced with ABS and PLA material at different printing speeds in 3D printer, J. Fac. Eng. Archit. Gazi Univ., 2022; 37(3): 1197–1211. https://doi.org/10.17341/gazimmfd.961981
16. Abdulridha H. H., Obaeed N. H., Jaber A. S. Optimization of fused deposition modeling parameters for polyethylene terephthalate glycol flexural strength and dimensional accuracy. Adv. Sci. Technol. Res. J., 2025; 19(4): 50–64. https://doi.org/10.12913/22998624/200088
17. Alsoufi M. S., Elsayed A. E., Surface roughness quality and dimensional accuracy–A comprehensive analysis of 100% infill printed parts fabricated by a personal/desktop cost-effective FDM 3D printer. Materials Sciences and Applications, 2018; 9: 11–40. https://doi.org/10.4236/msa.2018.91002
18. Dizon J. R. C., Gache C. C. L., Cascolan H. M. S., Cancino L. T., Advincula R. C. Post-processing of 3D-printed polymers. Technologies, 2021; 9(3): 1–37. https://doi.org/10.3390/technologies9030061
19. Torres J., Abo E., Sugar, A. J. Effects of annealing and acetone vapor smoothing on the tensile properties and surface roughness of FDM printed ABS components, Rapid Prototyp. J., 2023; 29(5): 921–934. https://doi.org/10.1108/RPJ-03-2022-0088
20. Mayville P. J., Petsiuk A. L., Pearce J. M. thermal post-processing of 3D printed polypropylene parts for vacuum systems. Journal of Manufacturing and

Materials Processing, 2022; 6(5):98. https://doi.org/10.3390/jmmp6050098

21. Kwon S., Hwang D. Understanding and resolving 3D printing challenges: A Systematic literature review. Processes, 2025; 13(6): 1–20. https://doi.org/10.3390/pr13061772
22. Zmarzły P., Gogolewski D., Kozior T. Design guidelines for plastic casting using 3D printing. J. Eng. Fibers Fabr., 2020; 15(6): 1–10. https://doi.org/10.1177/155892502091603
23. Vastola G., Sin W. J., Sun C. N., Sridhar N. Design guidelines for suppressing distortion and buckling in metallic thin-wall structures built by powder-bed fusion additive manufacturing. Mater. Des., 2022; 215: 110489.https://doi.org/10.1016/j.matdes.2022.110489
24. Kotliński J., Kęsy Z., Kęsy A., Jackson M., Parkin R. Dimensional deviations of machine parts produced in laser sintering technology. Int. J. Rapid Manuf., 2009; 1(1): 88–98.
25. Harun N., Kasim M., Abidin M.Z.Z., Izamshah R., Attan H., Ganesan H., A Study on surface roughness during fused deposition modelling: A review. Journal of Advanced Manufacturing Technology (JAMT), 2018; 12(1): 25–36. https://jamt.utem.edu.my/jamt/article/view/3922
26. Rahmati S., Vahabli E., Evaluation of analytical modeling for improvement of surface roughness of FDM test part using measurement results. Int. J. Adv. Manuf. Technol., 2015; 79(5–8): 823–829. https://doi.org/10.1007/s00170-015-6879-7
27. Jabłońska M., Łastowska O., Enhancing of surface quality of FDM moulded materials through hybrid techniques. Materials, 2024; 17(17): 4250. https://doi.org/10.3390/ma17174250
28. García-Martínez F., Carou D., de Arriba-Pérez F., García-Méndez S., Toward data-driven research: Preliminary study to predict surface roughness in material extrusion using previously published data with machine learning. Rapid Prototyp. J., 2023; 29(8): 1640–1652. https://doi.org/10.1108/RPJ-01-2023-0028
29. Cezarina A., Viorel P., Mitica A., Virgil T. Using 3D scanning in assessing the dimensional accuracy of mechanically machined parts. IOP Conf. Ser.: Mater. Sci. Eng., 2022; 1235: 012071. https://doi.org/10.1088/1757-899X/1235/1/012071
30. Pawlus P., Reizer R., Wieczorowski M. Comparison of results of surface texture measurement obtained with stylus methods and optical methods. Metrology and Measurement Systems, 2018; 25(3): 589–602. https://doi.org/10.24425/123894
31. Iwanicki W., Musiałek I., Osowski K., Olszak A., Kesy Z., Kęsy A. Experimental research concerning hydrodynamic clutches controlled by increasing distance between rotors. Adv. Sci. Technol. Res. J., 2021; 15(1): 218–229. https://doi.org/10.12913/22998624/132214
32. Kęsy A., Sarnik P. Przekładnia hydrokinetyczna z kołami łopatkowymi wykonanymi metodą szybkiego prototypowania. Napędy i Sterowanie, 2010; 2: 10–13.
33. Ishihara T., Emori R. I. Torque converter as a vibrator damper and its transient characteristics. SAE Technical Paper 1966; 660368. https://doi.org/10.4271/660368
34. Osowski K., Olszak A., Kęsy A., Kęsy Z. Application of the numerical calculations in the design process of hydrodynamic torque converter. Technical Transactions, 2017; 7(114): 183–190.
35. Milovanović D., Gordić D., Vukašinović V., Josijević M. Design method for hydrodynamic torque converter. Mobility and Vehicle Mechanics, 2020; 46(1): 1–12. https://doi.org/10.24874/mvm.2020.46.01.01
36. Luo Y., Zuo Z. G., Liu S. H., Fan H. G., Zhuge W. L. Numerical simulation of two-phase flows in a hydraulic coupling by solving VOF model. IOP Conf. Series: Materials Science and Engineering, 2013; 52: 1–7. https://doi.org/10.1088/1757-899X/52/7/072022
37. Hur N., Kwak M., Moshfeghi M., Chang C. S., Kang N. W. Numerical flow analyses of a two-phase hydraulic coupling. Journal of Mechanical Science and Technology, 2017; 31(5): 2307–2317. https://doi.org/10.1007/s12206-017-0427-3
38. Kęsy A., Numerical modelling of blade wheel geometry of hydrokinetic sub-assemblies (in Polish). Wydawnictwo Politechniki Radomskiej; 2008; 199.
39. Kosma Z. fundamentals of fluid mechanics [Podstawy mechaniki płynów]. Radom: Politechnika Radomska, Wydawnictwo Politechniki Radomskiej; 2002; 374.
40. Kęsy A. Mathematical model of hydrodynamic torque converter for vehicle power transmission system optimization. Int. J. Veh. Des., 2012; 59(1): 1–22. https://doi.org/10.1504/IJVD.2012.047777
41. Whitfield A., Wallace F. J., Patel A. Design of three element hydrokinetic torque converters. Int. J. Mech. Sci., 1983; 25(7): 485–497. https://doi.org/10.1016/0020-7403(83)90041-3
42. Kotwicki A. J. Dynamic models for torque converter equipped vehicles. SAE Technical Paper. 1982; 820393. https://doi.org/10.4271/820393
43. Kęsy Z., Control of hydrodynamic torque converter by means of working fluid [Sterowanie przekładni hydrokinetycznej cieczą roboczą]. Radom: Wydawnictwo Politechniki Radomskiej; 2003; 375.
44. Kotliński J. Printing Machine Parts [Drukowanie części maszyn]. Radom: Wydawnictwo Uniwersytetu Technologiczno-Humanistycznego im. Kazimierza Pułaskiego w Radomiu; 2018; 191.